International Journal of Nanomedicine

Dovepress
open access to scientific and medical research

Open Access Full Text Article

ORIGINAL RESEARCH

Enhancement of bioactivity of titanium carbonitride nanocomposite thin films on steels with biosynthesized hydroxyapatite

This article was published in the following Dove Press journal:
International Journal of Nanomedicine
1 October 2015
Number of times this article has been viewed

VV Anusha Thampi[1]
P Dhandapani[2]
Geetha Manivasagam[3]
B Subramanian[1]

[1]Electrochemical Materials Science Division, Central Electrochemical Research Institute, Karaikudi, [2]Corrosion and Materials Protection Division, Central Electrochemical Reserach Institute, Karaikudi, [3]Centre for Bio-Materials Science and Technology, VIT University, Vellore, India

Abstract: Thin films of titanium carbonitride (TiCN) were fabricated by DC magnetron sputtering on medical grade steel. The biocompatibility of the coating was further enhanced by growing hydroxyapatite crystals over the TiCN-coated substrates using biologically activated ammonia from synthetic urine. The coatings were characterized using X-ray diffraction, X-ray photoelectron spectroscopy, scanning electron microscopy (SEM)-energy dispersive spectroscopy, and Raman spectroscopy. The electrochemical behavior of the coatings was determined in simulated body fluid. In addition, hemocompatibility was assessed by monitoring the attachment of platelets on the coating using SEM. The wettability of the coatings was measured in order to correlate with biocompatibility results. Formation of a coating with granular morphology and the preferred orientation was confirmed by SEM and X-ray diffraction results. The hydroxyapatite coating led to a decrease in thrombogenicity, resulting in controlled blood clot formation, hence demonstrating the hemocompatibility of the coating.

Keywords: titanium carbonitride thin films, magnetron sputtering, ureolytic bacteria, biocompatibility

Background

The widespread use of austenitic (316 L) stainless steel (SS) as a bioimplant material may be attributed to the combination of its biocompatible nature, easy workability, good mechanical properties, and low cost. The major disadvantage of 316 L SS is crevice or pitting corrosion of the chromium oxide layer on continuous exposure to physiological solution. The metal ions leach out and accumulate in the body, leading to allergic reactions and ultimately resulting in failure of the implant material.[1,2] As the implant material starts to corrode, metal dissolution causes erosion, eventually leading to brittleness and fracture of the implant. Once the material fractures, corrosion is accelerated due to an increase in the amount of exposed surface area and loss of the protective oxide layer. If the metal fragments are not surgically extracted, further dissolution and fragmentation can occur, which may result in inflammation of the surrounding tissues.[3–7]

A breakthrough in the field of implants was achieved with the development of biocompatible Ti alloys as a tangible alternative to conventional 316 L SS. The major advantages of Ti-based alloys (Ti-13Nb-13zr, Ti-6Al-4V and Ti-6Al-7Nb) includes their excellent biocompatibility, elastic modulii close to that of bone, and absence of elements that often cause short-term and long-term adverse effects. However, the disadvantage of Ti alloys is their higher cost as compared with 316 L SS.[8]

An economic alternative to solve the problems in the field of implant materials would be to deposit thin film coatings onto 316 L SS to improve its resistance to corrosion and

Correspondence: Balasubramanian Subramanian
Electrochemical Materials Science Division, Central Electrochemical Research Institute, Karaikudi 630 006, India
Tel +91 45 6524 1538
Fax +91 45 6522 7713
Email subramanianb3@gmail.com

biocompatibility. Coating metal surfaces with ceramics is a good solution, as both wear and ion release can be reduced while high mechanical resistance and low cost are maintained. TiN films are pioneers for this purpose because they have high hardness with low wear coefficients and good biocompatibility. However, in modern biomedical applications, traditional TiN films cannot meet the stringent requirements as an implant material. Many methods have been proposed to improve the properties of TiN films, including incorporation of other elements, such as V, C, and Si.

Titanium carbonitride (TiCN) thin films are commonly used for cutting tool applications due to their chemical stability at elevated temperatures, high resistance to wear, good mechanical properties, and good resistance to corrosion.[9,10] Ti-X-N (where X indicates, eg, Cr, Si, C, or B) films can be formed on the surface of metal substrates by both chemical vapor and physical vapor deposition (PVD) techniques.[11–15] PVD includes a variety of vacuum deposition techniques for depositing thin films of condensed vapors of the desired material over a substrate surface. Generally, PVD methods comprise physical processes such as high temperature vacuum evaporation and plasma sputter deposition, whereas its counterpart, chemical vapor deposition, involves chemical reactions either in the traversing medium or on the substrate surface. PVD techniques have gained popularity due to their ability to form films that have appreciable hardness, improved corrosion resistance, high temperature resistance, good impact strength, excellent abrasion resistance, higher durability, and an ecofriendly nature.[16–19]

While the biocompatibility of Ti-X-N thin films on implantable steels is well documented, information on their ability to support cell proliferation and osseointegration is scarce. Cell-surface interactions play a crucial role in biomaterial application in the field of orthopedics.[20] Although the cytocompatibility of a biomaterial is strongly influenced by its chemical composition, surface topography plays a crucial role in cell-surface interactions.[21] Recent studies on the response of osteoblasts to controlled surface chemistries indicate that hydrophilic surfaces improve cell attachment and matrix synthesis and also osteogenic potency when compared with hydrophobic surfaces.[22–24] Growing a thin hydroxyapatite (HAp) layer over the coating can be considered as an ideal solution to improve the wettability of Ti-C-N coatings. HAp used as a coating for implants can exhibit varying levels of interaction with the biological environment. The crystallinity of the HAp-based coating has also been shown to control the rate of dissolution and appears to play a role in the initial cellular interaction with implant surfaces.[25]

In the present work, TiCN thin films were produced by reactive DC magnetron sputtering on 316 L SS substrates and assessed for bioimplant applications. HAp synthesized by a green method using biogenic ammonia was used to improve the bioactivity of the TiCN-coated steels; the bioactivity was checked in terms of surface properties and hemocompatibility for biomedical use.

Materials and methods

TiCN deposition and characterization

TiCN thin films were deposited on 316 L SS substrates by a reactive DC magnetron sputtering process in $Ar + N_2$ plasma. The sputtering unit had two plasma magnetron targets between which the substrate heater was continuously oscillating. First, 52 mm diameter and 3 mm thick high-purity Ti (99.95%) and graphite (99.99%) targets were sputtered for 2 hours in high purity Ar (99.999%) and N_2 (99.999%). Prior to deposition, the substrates were cleaned ultrasonically in water and acetone baths in succession and dried with a blower. The base pressure of the chamber before deposition was 8×10^{-6} mbar, and a total $Ar + N_2$ gas (sputtering) pressure of 5×10^{-3} mbar was maintained in the sputtering chamber. A 1:1 flow rate of N_2:Ar was maintained by two mass flow controllers attached to the sputtering system. The coatings were deposited at a substrate temperature of 400°C. For all the experiments, the sputtering powers were 150 W and 20 W for Ti and graphite targets, respectively.

X-ray diffraction (XRD) was used to identify the phase and structure of the deposited thin films (D8 Advance, Bruker, Karlsruhe, Germany), using Cu Kα radiation (0.1542 nm). The atomic bonding of the films was analyzed by Raman spectroscopy (InVia laser Raman microscope, Wotton-under-Edge, UK). Raman spectra measurements were carried out in the range of 200–2,000 cm^{-1}. The spectrometer was equipped with a charge-coupled device detector and a He-Ne laser (632.8 nm) operating at 18 mW and a total data point acquisition time of 10 seconds in the spectral region. The chemical composition of the films was analyzed by X-ray photoelectron spectroscopy (XPS). The XPS technique was used because of its effectiveness for characterization of the coatings, adsorbed phase, and nature of the chemical bonds. The microstructural features were studied by scanning electron microscopy (SEM, Tescan, Brno-Kohoutovice, Czech Republic) and the composition of the coating was analyzed using energy dispersive spectroscopy.

Synthesis of biogenic ammonia

Synthetic urine was prepared using the composition given in Table 1 and was inoculated with ureolytic bacteria. Rose Bengal was used as the indicator to detect formation of ammonia in the broth. The change in color of the broth from

Table 1 Composition of synthetic urine (for 1 L)

$CaCl_2 \cdot 2H_2O$	$MgCl_2 \cdot 2H_2O$	NaCl	KH_2PO_4	Na_2SO_4	KCl	NH_4Cl	Creatinine	Tryptone	Urea	pH
0.651 g	0.651 g	4.6 g	2.8 g	2.3 g	1.6 g	1.0 g	1.1 g	10 g	25 g	5.8

light yellow to pink indicates generation of ammonia from bacterial catalysis of urea by the urease enzyme. The pH of the broth was monitored at regular intervals with a pH meter (Eutech Instruments, Vernon Hills, IL, USA); subsequently, the concentration of biogenic ammonia was estimated by the indophenol method.[26] The biogenic ammonia was collected from the synthetic urine broth by centrifugation at 12,000 rpm for 30 minutes. In order to remove the bacterial cells along with other biogenic impurities, the supernatant solution was filtered using a filtration unit. The filtrate was used for synthesis of calcium HAp. Figure 1 shows a schematic representation of HAp synthesis using biogenic ammonia.

Synthesis of HAp

Calcium nitrate (4 g) was dissolved in 100 mL of distilled water and stirred using a magnetic stirrer. Dihydrogen potassium phosphate solution (1.7 g in 100 mL) was added dropwise to the above solution. The solution was then stirred for 30 minutes and, to optimize the pH, biogenic ammonia was added until the pH was raised up to 9.0. The sol was stirred for 3 hours at room temperature, and the temperature was then increased to 60°C with stirring for 3 hours. TiCN-coated substrates were suspended in the HAp precursor sol. The sol was allowed to stand with continuous stirring overnight. The HAp-deposited samples were taken out after 12 hours of stirring and dried at 80°C, followed by annealing at 300°C to obtain a thin layer of crystalline HAp on the TiCN/SS. The growth of a thin layer of HAp on the coated substrates was confirmed by XRD and XPS.

In vitro electrochemical characterization in simulated body fluid

Electrochemical measurements were performed in simulated body fluid with a Parstat 2273 advanced electrochemical system using a three-electrode cell, including a standard calomel electrode (KCl) as the reference electrode, Pt as the counter electrode, and the HAp/TiCN-coated 316 L SS substrate as the working electrode. The simulated body fluid solution was prepared as per the Kokubos method. The pH of the solution was maintained at 7.4. The corrosion behavior of all samples was monitored at 303 K. The sample was fixed on a holder with a 1 cm^2 window for interaction with the electrolyte. The corrosion behavior of any coating is directly proportional to its charge transfer resistance, R_{ct}. The higher the R_{ct} value, the higher the protection offered by the film coated onto the substrate.

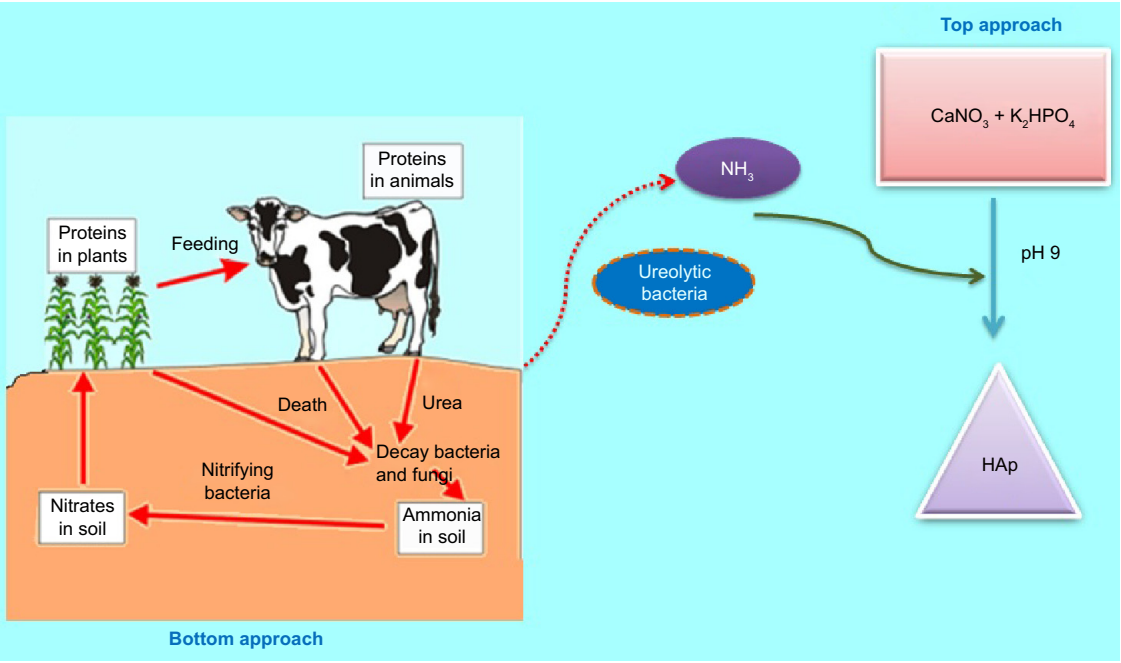

Figure 1 Schematic representation of biogenic HAp synthesis.
Abbreviation: HAp, hydroxyapatite.

The open-circuit potential was measured as a function of time until a stationary state was reached. Potentiodynamic polarization measurements were performed over the potential range of −200 to +200 mV with respect to the open-circuit potential at a scan rate of 1 mV per second. The corrosion current density (I_{corr}) was obtained using Tafel calculations. The polarization resistance (R_p) is a parameter correlated to the corrosion rate. The higher the polarization resistance, the lower will be the corrosion rate on the coating when exposed to simulated body fluid. The corrosion behavior is essentially related to the coated surface morphology and defects.

R_p can be related to I_{corr} by:

$$R_p = \beta_a \times \beta_c / 2.3 (\beta_a + \beta_c) I_{corr} \quad (1)$$

where R_p is the polarization resistance, β_a and β_c are the anodic and cathodic Tafel slopes, respectively, and I_{corr} is the corrosion current density.

The porosity of the coating was determined from the polarization resistance and corrosion potential, deduced from the potentiodynamic polarization technique, using the relationship shown in equation (2):

$$P = (R_{ps}/R_p) \times 10^{-|\Delta E_{corr}|/\beta_a} \quad (2)$$

where P is the total coating porosity, R_{ps} is the polarization resistance of the substrate, R_p is the polarization resistance of the coated steel, ΔE_{corr} is the difference between the corrosion potentials of the TiCN coated steel and the bare steel substrate, and β_a is the anodic Tafel slope of the substrate.

Wettability and hemocompatibility

The static contact angles were measured by the sessile drop method using a micrometric syringe. The images were analyzed using the VCA Optima program. The values of the contact angles correspond to the average of at least five experiments.

Hemocompatibility studies were carried out on HAp/TiCN/SS, TiCN/SS, and bare 316 L SS. Blood cell adhesion experiments were done to evaluate the surface thrombogenicity of the materials and to examine the interaction between blood and the materials in vitro, which also gives a measure of the compatibility of the material with the body. The specimen was first washed and incubated in human platelet-rich plasma for 60 minutes at 37°C. After incubation, the specimen was fixed with glutaraldehyde (2%) and critical point dried before gold sputtering for examination by SEM.[27]

Results and discussion

Material properties

A typical XRD pattern of the sputtered TiCN nanocomposite thin film is shown in Figure 2Ai. The pattern reveals that the coating is mainly composed of $TiC_{0.2}N_{0.8}$ (International Centre for Diffraction Data (ICDD) card 01-076-2484) with peaks along (111), (200), and (311). This result is consistent with the crystallization reports for TiCN synthesized by chemical routes and also by plasma spray techniques.[28,29] The maximum intensity peak was observed along (200) with a texture coefficient (T_c) value of 2.526. Using the Scherrer equation, the average grain size of the TiCN coating was estimated to be 20 nm.[30] A peak for the 316 L SS substrate (austenite Fe-γ) was also observed.[31] As reported by Schneider et al the (111) orientation of TiCN is normally favored during thin film growth.[32,33] The orientation is indicative of the growth of a columnar layer.[34] Consequently, the film would be more prone to corrosion in an aqueous electrolyte, because its columnar structure facilitates the penetration of ions through the coating whereas such accelerated corrosion can be avoided with an orientation along (200). Figure 2Aii shows the XRD pattern of HAp coated onto TiCN/SS (HAp/TiCN/SS). The peaks for HAp were found oriented along (002), (112), (410), and (153). The pattern was matched with Joint Committee on Powder Diffraction Standards (JCPDS) card 84-1998. The peaks corresponding to TiCN along (111), (200), and (311) was also observed in the pattern. It was noticed that annealing at 300°C to grow HAp crystals onto TiCN/SS did not alter the (200) texture of the TiCN coating. A profilometric (atomic force microscopy) image of TiCN/SS is shown in Figure 2B.

The Raman spectrum for the TiCN thin films revealed the C-N phase and Ti-N phase. Figure 3A shows the Raman spectrum for TiN. The peaks at 540 cm^{-1} and 310 cm^{-1} can be attributed to Ti-N. The low frequency peaks below 400 cm^{-1} are caused by acoustic phonons (LA) and the high frequency mode around 540 cm^{-1} is due to optical (TO) phonons.[35] The strong peaks at 310 cm^{-1} (LA) and at 540 cm^{-1} (TO) correspond to first-order Raman scattering. The intensities of the acoustic modes are comparable with the optical part of the spectra. This may be explained as follows: a substitutional impurity in a crystal with a sodium chloride structure still has local O_h symmetry, and the selection rules of this impurity induced scattering, showing that the phonons are contributing where the defect is at rest, in such a way that the intensities of the optical and acoustic modes are comparable.[36] It can be simply inferred that the scattering intensities in the acoustic branch are largely determined by vibrations of the heavy Ti, while the scattering in the optical branch is mainly due to the lighter

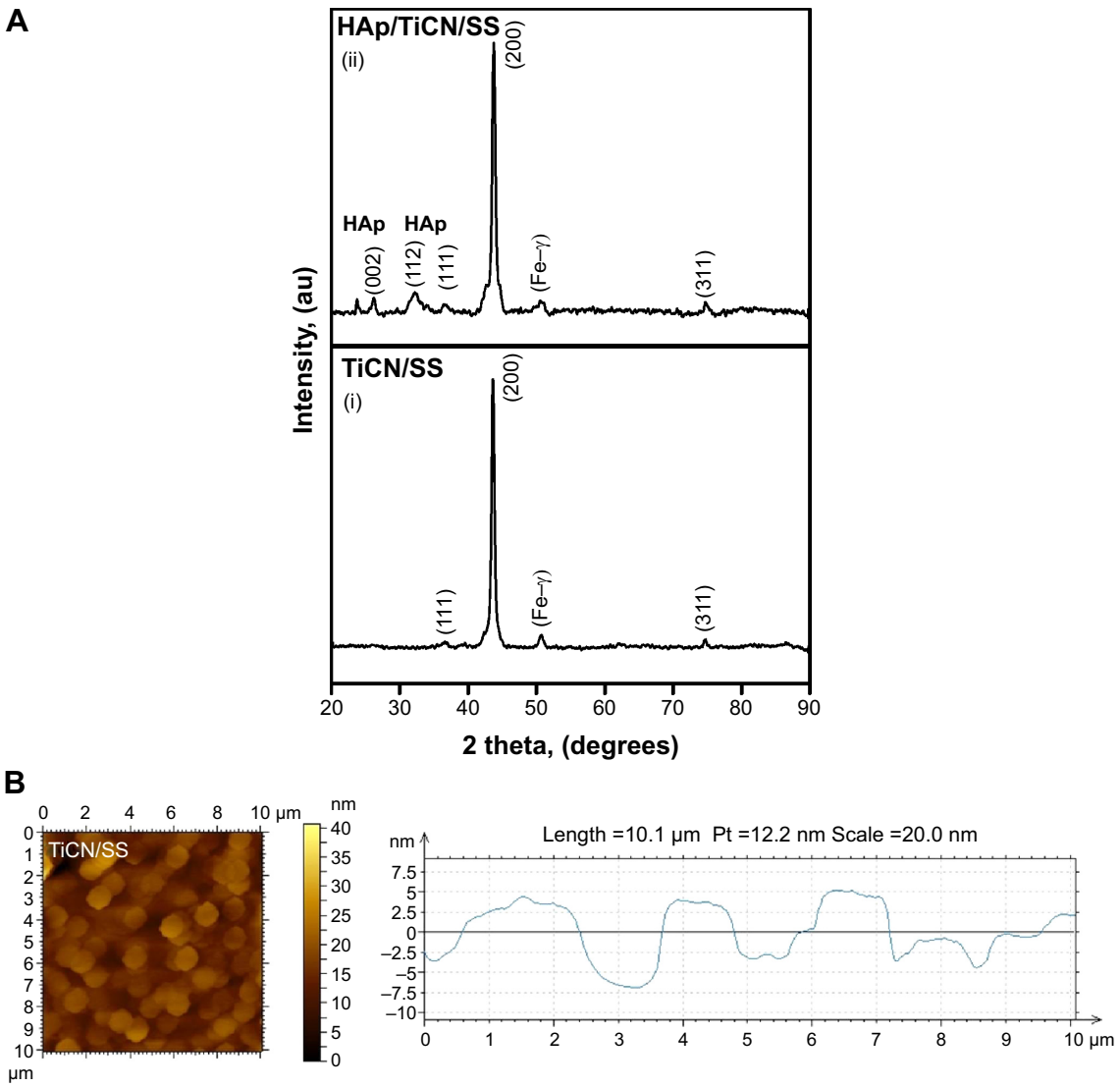

Figure 2 (**A**) X-ray diffraction pattern of (i) TiCN/SS and (ii) HAp/TiCN/SS. (**B**) Atomic force micrograph of TiCN on SS substrate.
Abbreviations: au, absorbance units; HAp, hydroxyapatite; SS, stainless steel; TiCN, titanium carbonitride.

N ion.[37] Figure 3B shows the Raman spectrum of C-N. Usually, the Raman spectra of graphitic films are characterized by a graphitic (G) band around 1,540 cm^{-1} and a disordered (D) band around 1,370 cm^{-1} in the spectral region within 1,000–1,800 cm^{-1}. The obtained spectrum shows a significant D ("disorder", at about 1,370 cm^{-1}) and G ("graphitic", at about 1,580 cm^{-1}) peaks, which confirm the presence of C phase. Figure 3C shows the Raman spectrum of TiCN thin film composed of crystalline grains and C-N phase.[36] The presence of the D and G bands at 1,364 and 1,583 cm^{-1}, respectively, correspond to the presence of aromatic six-membered sp^2 clusters and the sp^2 C-C bonds.[31] The peak between 540 and 600 cm^{-1} may be attributed to Ti-N. A slight shift in the peak as compared with the original Ti-N spectra can be observed. This shift may be due to the inclusion of graphitic carbon.

Figure 4 shows the XPS core level spectra of the TiCN thin film on SS substrate. The Ti 2p exhibits four peaks located at the line positions of 455.3, 457.9, 461.2, and 463.5 eV. The spectrum consists of Ti $2p_{3/2}$ and Ti $2p_{1/2}$ due to spin-orbit coupling. The binding energy values of Ti 2p at 457.9 eV and 463.5 eV correspond to TiCN, whereas the peaks positioned at 455.3 eV and 461.2 eV are attributed to Ti-C.[38,39] The C 1s peak includes three components. The peak with most intensity at 284.6 eV can be assigned to "surface" carbon.[40] The peak at 286.2 eV is assigned emission from sp^2 and sp^3 carbon.[41] A lower intensity peak at 288.4 eV is also observed in the C 1s spectrum, which can be assigned to metal carbonates (Ti-O-C=O) formed on the surface of the thin film. The N 1s spectrum shows a peak at 396.5 eV corresponding to Ti-N.[41] Metal oxide and metal carbonate peaks were also observed

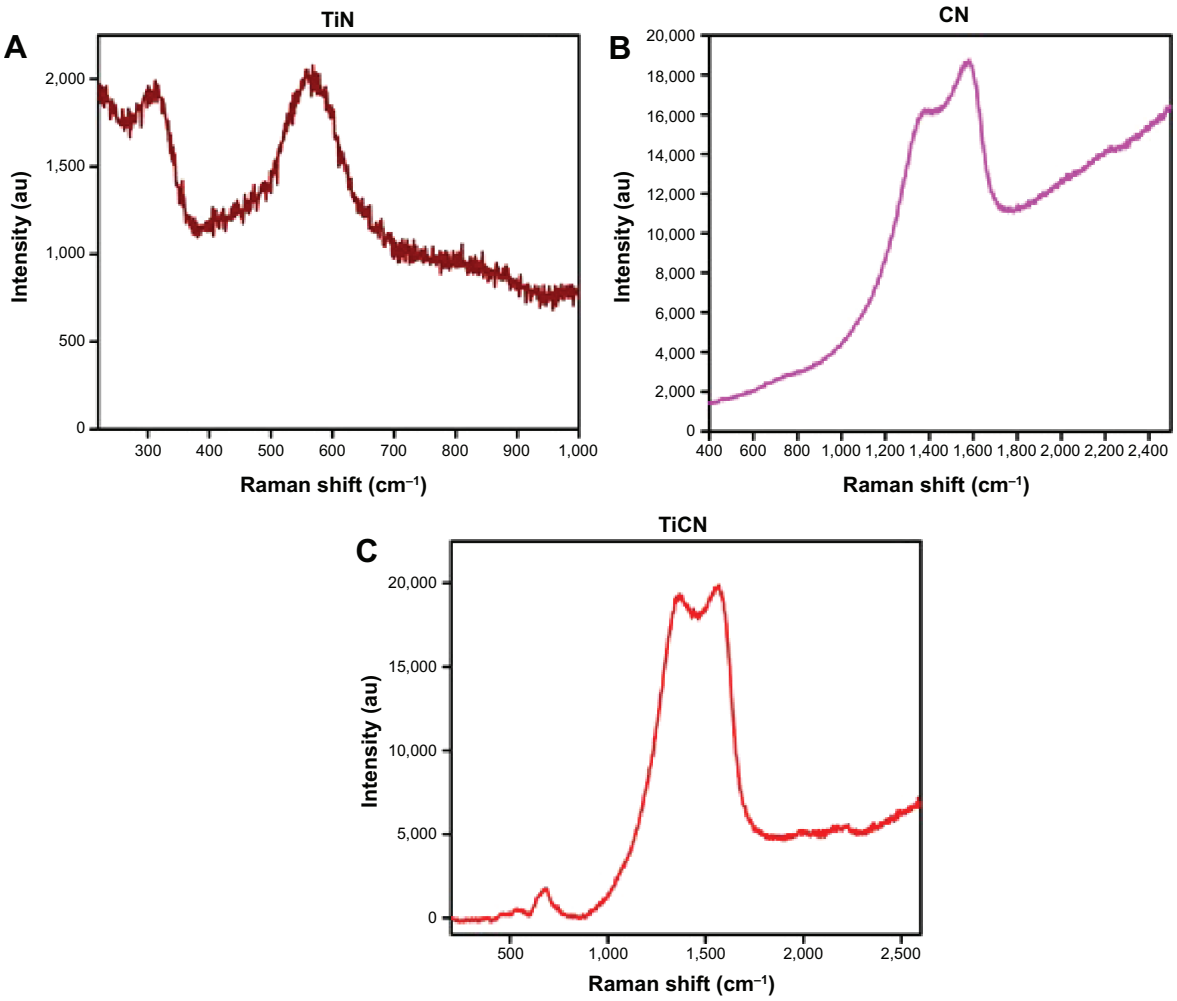

Figure 3 Raman spectra for (**A**) TiN, (**B**) CN, and (**C**) TiCN.
Abbreviations: au, absorbance units; TiCN, titanium carbonitride.

from the O 1s spectrum at 529.64 and 532 eV, respectively, and the peaks are due to the surface oxidation of TiCN thin film on exposure to atmospheric oxygen.[42]

Figure 5 shows the XPS spectra of HAp/TiCN/SS. Peaks corresponding to P 2p, Ca 2p, and O 1s were observed in addition to those for Ti 2p, N 1s, and C 1s in the survey spectrum. The peaks for Ti 2p, N 1s, and C 1s were in agreement with those for TiCN/SS as mentioned above.[10] The stoichiometric ratio of Ca/P was obtained from the spectrum and found to be 1.65, which is close to the standard value (1.67). In the O 1s spectrum, two obvious peaks were observed. The peak due to metal oxides was positioned at 529.9 eV whereas the second peak at 537.9 eV was due to oxygen associated with the phosphate group in HAp. The binding energies of HAp/TiCN/SS are given in Table 2.

A morphological and chemical composition analysis was carried out by SEM-energy dispersive spectroscopy after sputter-covering the TiCN-coated substrates by a thin Au layer in order to avoid charging effects. The energy dispersive spectrum (shown in Figure 6A and B) of the film revealed the presence of Ti, C, and N. The SEM images of the coatings deposited onto the 316 L SS substrates revealed dense, homogeneous, and granular morphologies.

In vitro corrosion studies

The corrosion behavior of the TiCN-coated samples was examined using DC potentiodynamic polarization and AC electrochemical impedance measurements. Figure 7A and B shows the Nyquist plots and Tafel polarization curves for the tested samples (TiCN/SS and bare 316 L SS) in simulated body fluid solution, with the composition given in Table 3. The impedance measurements were made at open circuit potential (OCP) by applying an AC signal of 10 mV in the frequency range of 100–10 mHz. At higher frequencies, the interception of the real axis in the Nyquist plot is ascribed to the solution resistance (R_s), and at lower frequencies it gives the R_{ct}.

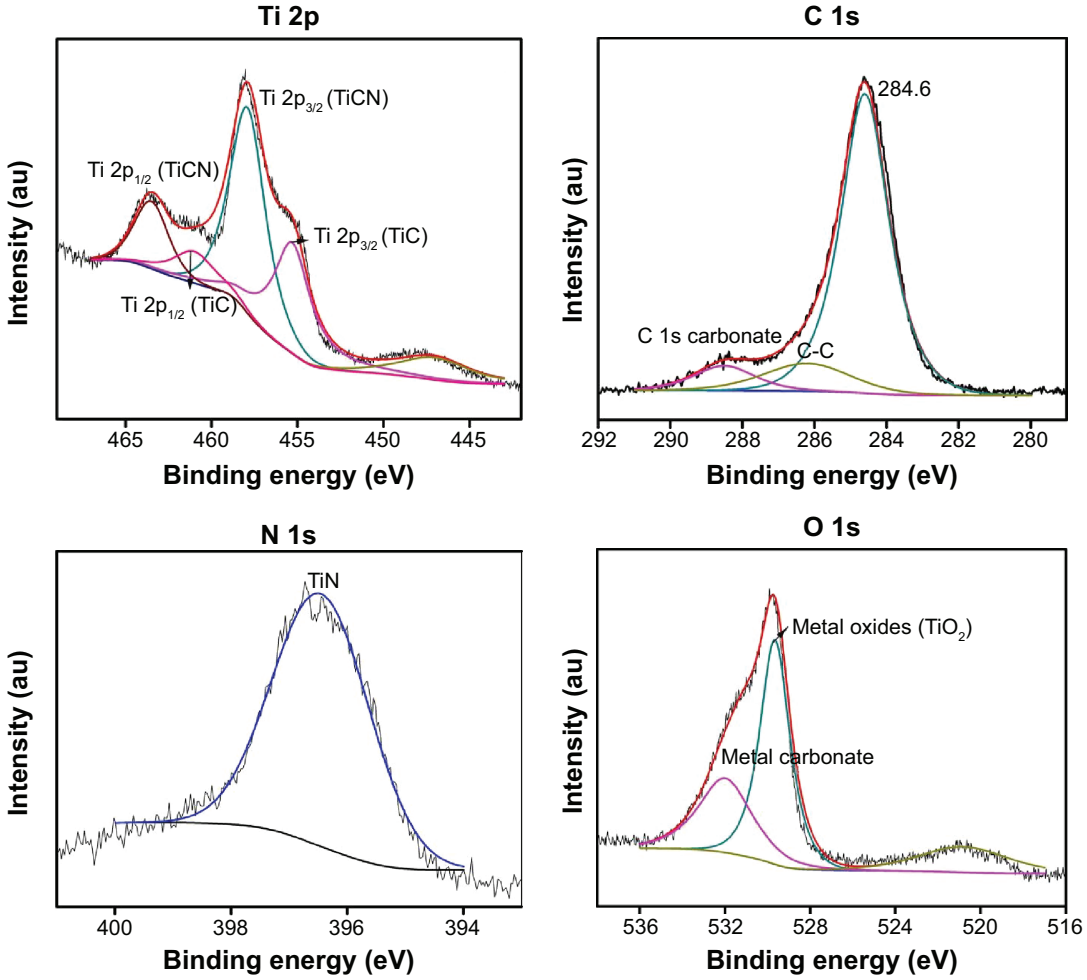

Figure 4 X-ray photoelectron spectroscopy pattern for TiCN/SS.
Abbreviations: au, absorbance units; SS, stainless steel; TiCN, titanium carbonitride; TiC, titanium carbide; TiN, titanium nitride.

A higher R_{ct} value indicates better corrosion resistance, and was observed in the case of TiCN/SS as compared with the bare 316 L SS.[27] The improvement in corrosion resistance of the coated sample may be accounted for by the preferred orientation of TiCN thin film along (200), as observed from the XRD pattern. Unlike a columnar morphology, this preferred orientation has rendered a granular morphology for the TiCN thin film (as observed in the SEM image) which minimizes the direct diffusion path of the electrolyte.

The corrosion current densities were obtained from the polarization curves by extrapolation of the cathodic branch of the polarization curves to the corrosion potential. Table 4 show the calculated values for the corrosion parameters from the Tafel and Nyquist plots. From the Tafel plot, a positive shift in the E_{corr} value can be observed, implying that the TiCN coating improves the corrosion resistance of the SS substrate. The polarization resistance and R_{ct} values of the coated sample were found to be higher in comparison with the blank SS substrate. A protective efficiency of 99.25% for the TiCN-coated sample was observed.

The electrochemical impedance spectroscopy for HAp/TiCN/SS was also studied to analyze the corrosion behavior of the TiCN/SS substrate after growth of HAp onto it. It was observed that the R_{ct} value of HAp grown TiCN/SS is lesser than that of TiCN/SS. A double semicircle, which is characteristic of a failed coating, was observed in the Nyquist plot (Figure 7A). This behavior may be due to the nonuniform growth of the HAp layer onto TiCN/SS. This might suggest that there is an additional electrochemical process other than the interfacial charge transfer reaction due to the presence of a porous thin layer adjacent to the TiCN/SS surface. These additional loops suggest that a second time constant is present.[43]

Wettability and hemocompatibility

The hydrophilic nature of the bare 316 L SS samples was changed to hydrophobic on coating with TiCN. Bare 316 L SS

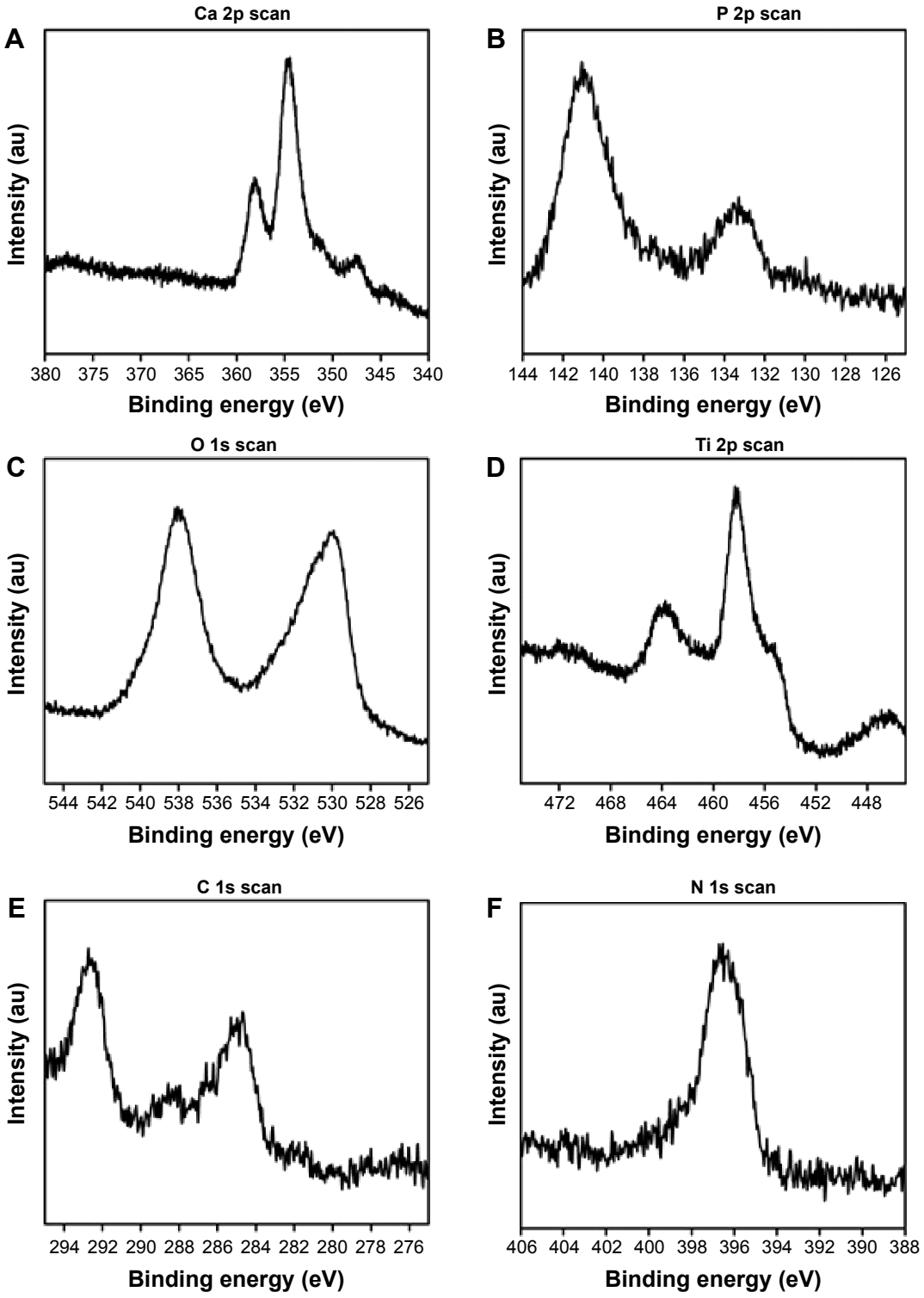

Figure 5 X-ray photoelectron spectroscopy (XPS) pattern of HAp/TiCN/SS.
Notes: The figure shows the XPS spectra of each component present in HAp/TiCN: (**A**) Calcium (Ca) 2p; (**B**) Phosporous (P) 2p; (**C**) Oxygen (O) 1s; (**D**) Titanium (Ti) 2p; (**E**) Carbon (C) 1s; (**F**) Nitrogen (N) 1s.
Abbreviations: au, absorbance units; HAp, hydroxyapatite; SS, stainless steel; TiCN, titanium carbonitride.

Table 2 Electron binding energy (eV) of the samples

Sample	Ti $2p_{3/2}$	Ti $2p_{1/2}$	C 1s	N 1s	Ca $2p_{1/2}$	Ca $2p_{3/2}$	P $2p_{3/2}$	P $2p_{1/2}$	O 1s
HAp/TiCN/SS	458.1	463.7	284.8	396.4	354.5	347.3	133.2	140.9	530.3

Abbreviations: HAp, hydroxyapatite; SS, stainless steel; TiCN, titanium carbonitride.

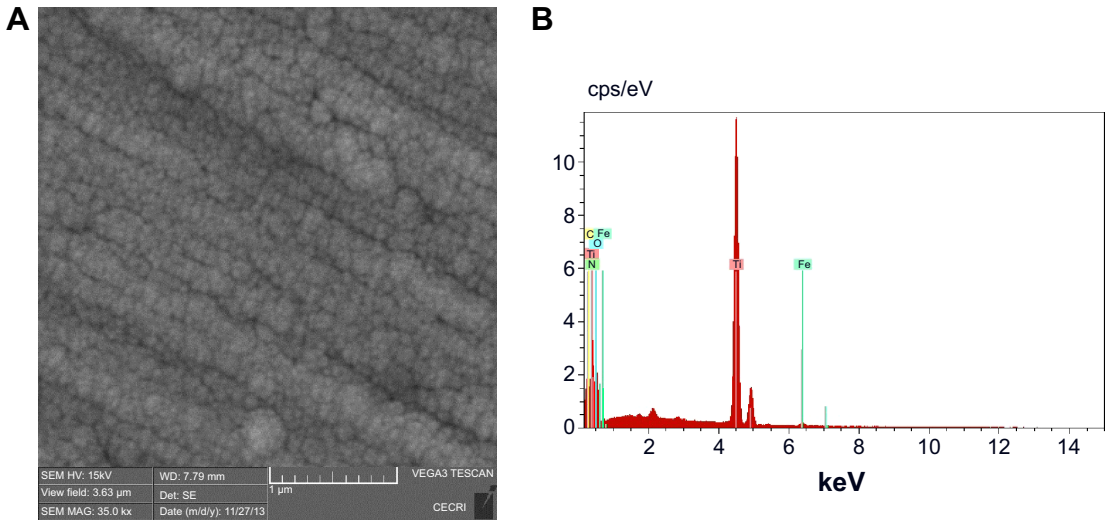

Figure 6 (**A**) Scanning electron micrograph of TiCN/SS and (**B**) energy dispersive spectroscopic image of TiCN/SS.
Abbreviations: SS, stainless steel; TiCN, titanium carbonitride.

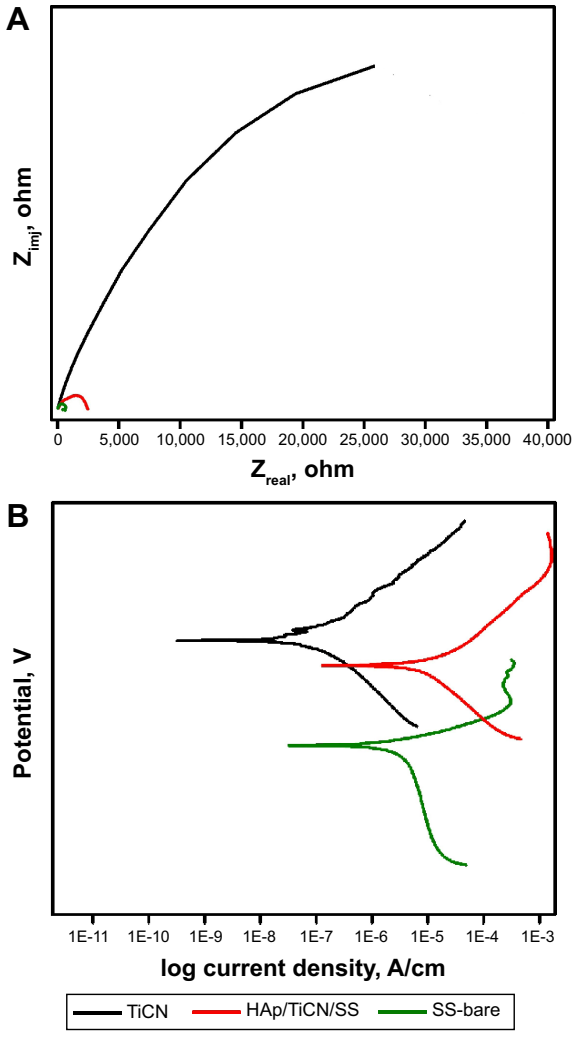

Figure 7 (**A**) Nyquist plot of SS, TiCN/SS, and HAp/TiCN/SS. (**B**) Tafel plot of SS, TiCN/SS, and HAp/TiCN/SS.
Abbreviations: HAp, hydroxyapatite; SS, stainless steel; TiCN, titanium carbonitride.

samples coated with TiCN, Ti-N, and C-N were analyzed to study the surface wettability. Figure 8 shows a comparison between the contact angles of TiCN with Ti-N, C-N, and the bare substrate, and it can be seen that the initial contact angle between the water droplet and the SS bare substrate surface is 68 degrees, whereas after coating with TiCN it increases to 122 degrees.

The morphology of the adherent blood cells were observed by SEM (Figure 9). A considerable reduction in thrombus (blood cell aggregation) formation along with formation of a fibrin fiber network was observed in the order TiCN/SS > bare 316 SS > HAp/TiCN/SS. More fibrin fibers were formed on the TiCN-coated substrates than on the bare metal surface because of the hydrophobic nature of the coating. Adsorption of fibrinogen is heavily favored on hydrophobic surfaces and consequently results in platelet adhesion. Deposited platelets catalyze the activation of coagulation factors and prothrombin, leading to formation of thrombin. Thrombin activates more platelets, creating a positive feedback loop. Thrombin cleaves fibrinogen into

Table 3 Composition of simulated body fluid

Sl No	Reagent	Amount
1	NaCl	7.996 g
2	$NaHCO_3$	0.350 g
3	KCl	0.224 g
4	$K_2HPO_4 \cdot 3H_2O$	0.228 g
5	$MgCl_2 \cdot 6H_2O$	0.305 g
6	1 mol/m^3 HCl	40 cm^3
7	$CaCl_2$	0.278 g
8	Na_2SO_4	0.071 g
9	$(CH_2OH)_3CNH_2$	6.057 g
10	1 mol/m^3 HCl	Appropriate amount to adjust pH

Table 4 Electrochemical studies on TiCN-coated SS and bare 316 L SS

Sample	E_{corr} (mV)	I_{corr} (μA)	β_a (mV)	β_b (mV)	Polarization resistance (Ω)	Corrosion rate $\times 10^{-6}$ (mpy)	R_{ct} (Ω)	Protective efficiency
Bare SS	−341	13.12	670	235	5.765×10^{3}	6.24	3,136	–
TiCN/SS	−130	0.098	103	119	2.44×10^{5}	3.264×10^{-3}	6.226×10^{4}	99.25
HAp/TiCN/SS	−223	0.463	210	554	4.46×10^{4}	4.22	5.674×10^{3}	85.6

Abbreviations: HAp, hydroxyapatite; SS, stainless steel; TiCN, titanium carbonitride.

fibrin monomers which then polymerize to form a fibrous mesh. This fibrous mesh stabilizes the platelet plug and forms the blood clot. The SEM images of blood cell adhesion on TiCN/SS clearly show the fibrin mesh (Figure 9). On the other hand, there was little thrombus formation on HAp/TiCN/SS, which may be attributed to immobilization of albumin by HAp. It is well known that the association of albumin protein with various materials has an antithrombogenic effect due to the negative charge of the protein.[44,45]

Conclusion

TiCN thin films were prepared by reactive DC magnetron sputtering on medical grade steels. The microstructure of the thin film was analyzed by XRD and Raman spectroscopy, which confirmed the presence of TiCN. The observed preferred orientation along (200) renders a granular morphology which minimizes the diffusion path of the electrolyte through the coating reaching the substrate, unlike the columnar structure. This was clearly observed from the Nyquist plot, where a higher R_{ct} value was observed for TiCN-coated 316 L SS as compared with the bare substrate. A decrease in R_{ct} value after coating with biogenic HAp was observed, which was due to the nonuniformity of crystal growth by the dip-coating method and the porous nature of the biomineral. The increased fibrin mesh formation in the TiCN thin film upon contact with blood cells was due to the hydrophobic

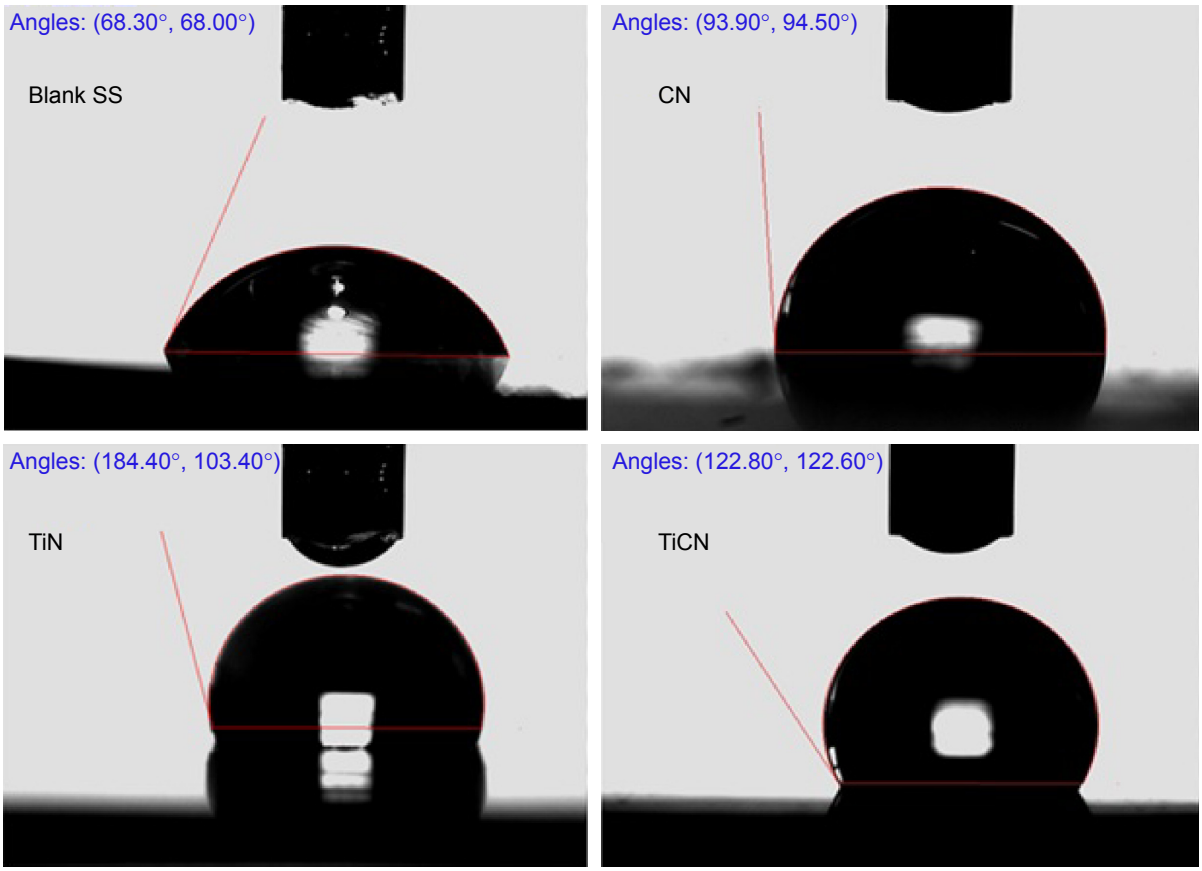

Figure 8 Wettability studies on bare SS, TiN, CN, and TiCN.
Abbreviations: SS, stainless steel; TiCN, titanium carbonitride; TiC, titanium carbide; CN carbonitride.

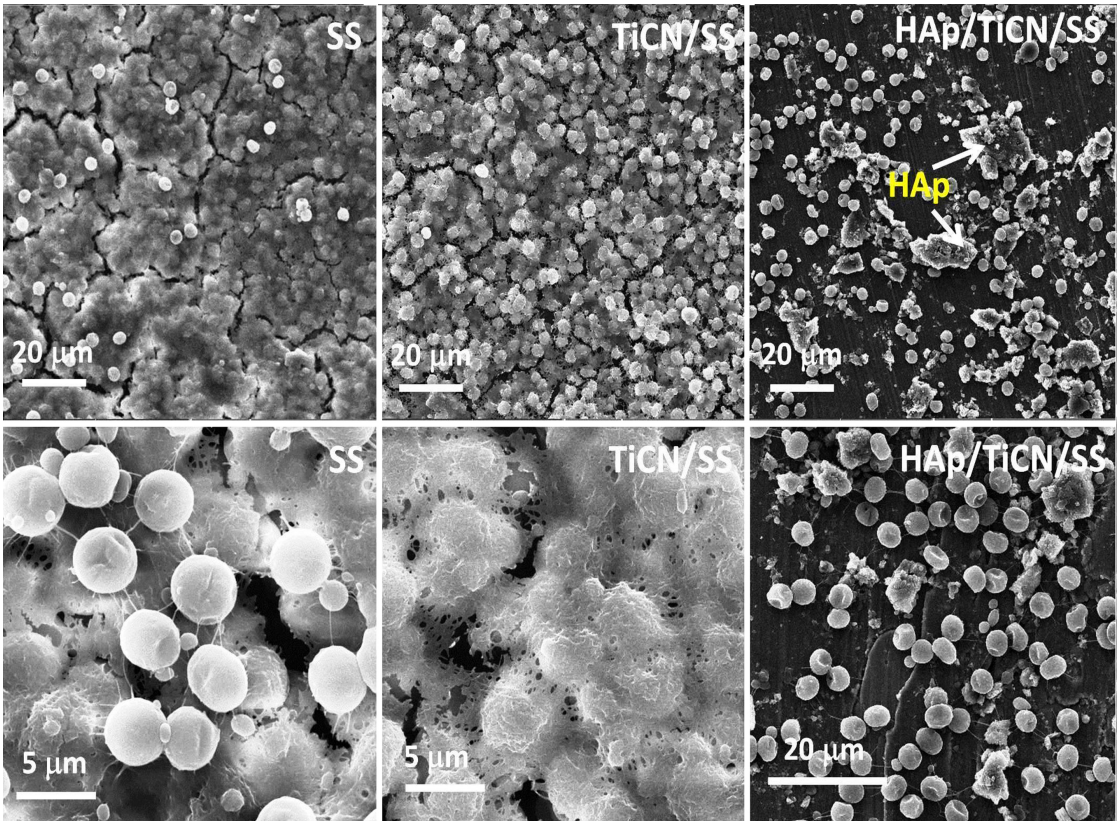

Figure 9 Hemocompatibility studies for SS, TiCN/SS, and HAp/TiCN/SS.
Abbreviations: HAp, hydroxyapatite; SS, stainless steel; TiCN, titanium carbonitride.

nature of the coated surface, which favors the formation of thrombus, whereas the probability of clot formation was found to decrease to a greater extent when HAp was grown over TiCN. An early stage of blood cell activation was observed with pseudopod formation on HAp/TiCN, while the further steps in blood clot formation were controlled, which may be due to the enhanced hemocompatibility of HAp. This study suggests that TiCN/HAp can provide better surface properties when used as a biocompatible coating on implant material.

Acknowledgments

The authors thank the Department of Atomic Energy, Board of Research in Nuclear Sciences, Mumbai, for their research grant (2012/37P/38/BRNS) to carry out this work, and Johnson and Johnson for sponsoring this paper for publication.

Disclosure

The authors declare no conflicts of interest in this work.

References

1. Antunes RA, Rodas ACD, Lima NB, Higa OZ, Costa I. Study of the corrosion resistance and in vitro biocompatibility of PVD TiCN-coated AISI 316 L austenitic stainless steel for orthopedic applications. *Surf Coat Technol.* 2010;205:2074–2081.
2. Gurappa I. Characterization of different materials for corrosion resistance under simulated body fluid conditions. *Mater Character*. 2002;49:73–79.
3. Serro AP, Completo C, Colaço R, et al. A comparative study of titanium nitrides, TiN, TiNbN and TiCN, as coatings for biomedical applications. *Surf Coat Technol.* 2009;203:3701–3707.
4. Manivasagam G, Dhinasekaran D, Rajamanickam A. Biomedical implants: corrosion and its prevention – a review. *Recent Patents on Corrosion Science*. 2010;2:40–54.
5. Pazzaglia UE, Beluffi G, Colombo A, Marchi A, Coci A, Ceciliani L. Myositis ossificans in the newborn – a case report. *J Bone Joint Surg Am*. 1986;68:456–458.
6. Williams DF. Biomaterials and tissue engineering in reconstructive surgery. *Sadhana*. 2003;28:563–574.
7. Urban RM, Jacobs JJ, Gilbert JL, Galante JO. Migration of corrosion products from modular hip prostheses. Particle biomedical implants: corrosion and its prevention microanalysis and histopathological findings. *J Bone Joint Surg Am*. 1994;76:1345–1359.
8. Antunes RA, De Assis S, Lorenzetti SG, ZazucoHiga O, Costa I. Comparison of in vitro corrosion behaviour and biocompatibility of Ti-13zr-13nb and passivated 316l stainless steel coated with TiCN. Presented at the 18th International Congress Of Mechanical Engineering, Ouro Preto, Brazil, November 6–11, 2005.
9. Jeon ET, Joardar J, Kang S. Microstructure and tribo-mechanical properties of ultrafine Ti(CN) cermets. *Int J Refract Met Hard Mater.* 2002;20:207–211.
10. Chen R, Tu JP, Liu DG, Mai YJ, Gu CD. Microstructure, mechanical and tribological properties of TiCN nanocomposite films deposited by DC magnetron sputtering. *Surf Coat Technol*. 2011;205:5228–5234.
11. Fainer NI, Golubenko AN, Rumyantsev YM, Kesler VG, Maksimovskii EA, Kuznetsov FA. Preparation of nanocrystalline titanium carbonitrides coatings using $Ti(N(Et)_2)_4$. *Glass Physics and Chemistry*. 2011;37 Pt 3:322–329.

12. Gong Y, Tu R, Goto T. Microstructure and preferred orientation of titanium nitride films prepared by laser CVD. *Mater Trans.* 2000;50 Pt 8: 2028–2034.
13. Bonetti RS, Wiprachtiger H, Mohn E. Chemical vapour deposition of titanium carbonitride at moderate temperature: properties and applications. *Metal Powder Report*. 1990;45 Pt 12:837–840.
14. Pierson HO. Titanium carbonitrides obtained by chemical vapour deposition. *Thin Solid Films*. 1977;40:41–47.
15. Balasubramanian S, Ramadoss A, Kobayashi A, Muthirulandi J. Nanocomposite TiSiN coatings deposited by reactive DC magnetron sputtering for biomedical applications. *J Am Ceram Soc*. 2012;95(9): 2746–2752.
16. Hsu CH, Lin CK, Huang KH, Ou KL. Improvement on hardness and corrosion resistance of ferritic stainless steel through PVD-(Ti, Cr)-N coatings. *Surf Coat Technol*. 2013;231:380–384.
17. Uglov VV, Remnev GE, Kuleshov AK, Saltymakov MS. Modification of (Ti, Cr)N coatings on a hard alloy under the action of high-power pulsed ion beams. *Inorganic Materials: Applied Research*. 2011;2 Pt 3: 242–246.
18. Oliveira C, Escobar Galindo R, Palacio C, et al. Surface characterisation of Ti-Si-C-O-N coatings for orthopedic devices: XPS and Raman spectroscopy. *Solid State Sci.* 2011;13:95–100.
19. Chang Y-Y, S Yang S-J, D Wang D-Y. Characterisation of TiCr(CN)/amorphous carbon coatings synthesized by a cathodic arc deposition process. *Thin Solid Films*. 2007;515:4722–4726.
20. Ager MJ, Zilkens C, Zanger K, Krauspe R. Significance of nano- and microtopography for cell-surface interactions in orthopaedic implants. *J Biomed Biotechnol*. 2007;2007:69036.
21. Meredith DO, Eschbach L, Riehle MO, Curtis AS, Richards RG. Microtopography of metal surfaces influence fibroblast growth by modifying cell shape, cytoskeleton, and adhesion. *J Orthop Res*. 2007;25: 1523–1533.
22. Jager M, Urselmann F, Witte F, et al. Osteoblast differentiation onto different biometals with an endoprosthetic surface geometry in vitro. *J Biomed Mater Res A*. 2008;86A:61–75.
23. Redey SA, Nardin M, Bernache-Assolant D, et al. Behavior of human osteoblastic cells on stoichiometric hydroxyapatite and type A carbonate apatite: role of surface energy. *J Biomed Mater Res*. 2000;50: 353–364.
24. Zhao G, Schwartz Z, Wieland M, et al. High surface energy enhances cell response to titanium substrate microstructure. *J Biomed Mater Res A*. 2005;74 Pt 1:49–58.
25. Chang YL, Stanford CM, Wefel JS, Keller JC. Osteoblastic cell attachment to hydroxyapatite-coated implant surfaces in vitro. *Int J Oral Maxillofac Implants*. 1999;14 Pt 2:239–247.
26. Dhandapani P, Siddarth AS, Kamalasekaran S, Maruthamuthu S, Rajagopal G. Bio-approach: ureolytic bacteria mediated synthesis of ZnO nanocrystals on cotton fabric and evaluation of their antibacterial properties. *Carbohydr Polym*. 2014;103:448–455.
27. Subramanian B, Dhandapani P, Maruthamuthu S, Jayachandran M. Biosynthesis of calcium hydroxylapatite coating on sputtered Ti/TiN-nano multilayers and their corrosion behavior in simulated body solution. *J Biomater Appl*. 2012;26:687–705.
28. Feng X, Shi LY. Novel chemical metathesis route to prepare TiCN nanocrystallites at low temperature. *Mater Chem Phys.* 2005;94 Pt 1: 58–61.
29. Zhu L, He J, Yan D, et al. Titanium carbonitride thick coating prepared by plasma spray synthesis and its tribological properties. *Chin Sci Bull.* 2007;52:1849–1855.
30. Klug HP, Alexander LE. *X-ray Diffraction Procedures: For Polycrystalline and Amorphous Materials*. New York, NY, USA: Wiley Interscience; 1974.
31. Antunes RA, Rodas ACD, Lima NB, Higa HZ, Costa I. Study of the corrosion resistance and in vitro biocompatibility of PVD TiCN-coated AISI 316 L austenitic stainless steel for orthopedic applications. *Surface and Coatings Technology.* 2010;205:2074–2081.
32. Schneider JM, Voevodin A, Rebholz C, et al. *Surf Coat Technol.* 1995; 74:312–321.
33. Yang D, Liu C, Liu X, Qi M, Lin G. EIS diagnosis on the corrosion behavior of TiN coated NiTi surgical alloy. *Curr Appl Phys.* 2005;5:417–421.
34. Chen CC, Liang XT, Tse WS, Chen IY, Duh JG. Raman spectra of titanium nitride thin films. *Chin J Phys.* 1994;32(2):205–210.
35. Spengler W, Kaiser R, Bilz H. Resonant Raman scattering in a superconducting transition metal compound TiN. *Solid State Commun*. 1975; 17:19–22.
36. Sánchez-López JC, Abad MD, Carvalho I, et al. Influence of silver content on the tribomechanical behavior on Ag-TiCN bioactive coatings. *Surf Coat Technol.* 2012;206:2192–2198.
37. Okrój W, Walkowiak-Przybyło M, Rośniak-Bak K, Klimek L, Walkowiak B. Comparison of microscopic methods for evaluating platelet adhesion to biomaterial surfaces. *Acta Bioeng Biomech*. 2009;11: 45–49.
38. Cheng Y, Zheng YF. Characterisation of TiN, TiC and TiCN coatings on Ti-50.6 at.% Ni alloy deposited by PIII and deposition technique. *Surf Coat Technol*. 2007;201:4909–4913.
39. Devia Narvaez DM, Gonzalez Carmona JM, Ruden Munoz A. Interface description using computational methods and tribological characteristic of TiN/TiC films prepared by reactive pulse arc evaporation technique. *Revista Mexicana de Física*. 2013;59:90.
40. Dobrzanski LA, Zukowska LW, Kubacki J, Golombek K, Mikula J. XPS and AES analysis of PVD coatings. *Archives of Materials Science and Engineering*. 2008;22:99–102.
41. Kocourek T, Jelinek M, Kadlec J, Popov C, Santoni A. Thin TiCN films prepared by hybrid magnetron-laser deposition. *Plasma Processes and Polymers*. 2007;4:651–654.
42. Thermo Scientific. [webpage on the Internet]. *Oxygen*. Available from http://xpssimplified.com/elements/oxygen.php. Accessed 20 April 2015.
43. Karbovskii VL, Kurgan NA, Dubok VA, et al. Morphology and spectral behavior of hydroxyapatite nanocrystalline coatings obtained by gas detonation deposition. *Funct Mater*. 2012;19:297.
44. Chen Y, Jepson WP. EIS measurement for corrosion monitoring under multiphase flow conditions. *Electrochim Acta.* 1999;44:4453–4464.
45. Heemskerk JW, Bevers EM, Lindhout T. Platelet activation and blood coagulation. *Thromb Haemost*. 2002;88:186–193.